Dynamically Reconfigurable Tactile Sensor for Robotic Manipulation

Tae Myung Huh, Hojung Choi, Simone Willcox, Stephanie Moon, and Mark R. Cutkosky

***Abstract*—We present a tactile sensor intended for manipulation by mobile robots, e.g., in the home. The surface consists of an array of small, rounded bumps or "nibs," for reliable traction on objects like wet dishes. When the nibs contact a surface they deflect, and capacitive sensors measure the corresponding local normal and shear stresses. A feature of the sensor is the ability to reconfigure dynamically depending on which combinations of sensing elements it samples. By interrogating different combinations of elements the sensor can detect and distinguish between linear and rotational sliding, and other dynamic events such as making contact. These dynamic events, combined with the sensed grasp and load forces, are useful for acquiring objects and performing simple in-hand manipulations. A proposed slip detection method estimates minimum required grasping force with an error less than 1.5 N and uses tactile controlled rotational slips to reorient an unknown weight/surface object with 78% success rate.**

***Index Terms*—Force and Tactile Sensing, Perception for Grasping and Manipulation, Dexterous Manipulation**

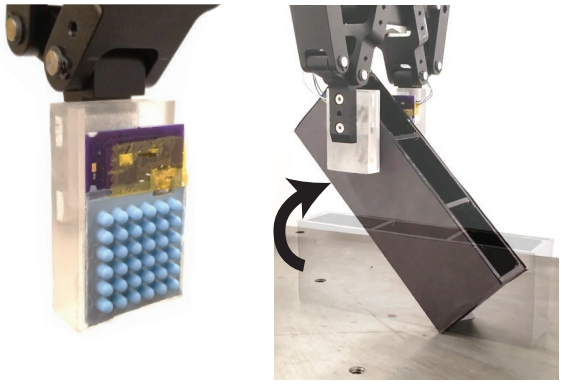

Fig. 1: Sensing pad is coated with bumps to grip in wet conditions and measure normal and shear pressures. Different dynamic interrogation schemes allow the robot to distinguish between linear and rotational sliding.

I. Introduction

CONSIDER robots working at home. A quintessential task is preparing meals and cleaning up dirty dishes. Robots will handle delicate or slippery items, such as food and dirty dishes, in a cluttered environment originally designed for humans.

Humans achieve such manipulation tasks effortlessly using multimodal information from tens of thousands of mechanoreceptors in their hands [1]. Ensembles of diverse slowly adapting (SA) and fast adapting (FA) mechanoreceptors play a pivotal role for tasks such as object recognition, grasp force control, and response to contacts [1], [2]. The processing of large number of mechanoreceptors is achieved partially from a convergence of neural connections; tens of mechanoreceptors may be connected to a single neuron [3]. The receptive fields associated with these neural bundles are intermingled, allowing hyper-acuity [3].

In robotic manipulation, multimodal sensing has also been studied to respond to diverse combinations of contact events and to combine mechanical and thermal sensing, with examples dating from the 1980s [4] to recent years [5]–[11]. In most cases, these multimodal sensors utilize different transducers for static or dynamic quantities; however with sufficiently fast sampling and sensor bandwidth it is also possible to use a single transduction approach [5], [12].

An additional interest for manipulation in cluttered environments is to permit in-hand manipulation, which can increase the dexterity available with an under-actuated hand. Examples include rotational sliding and compliant accommodation to forces from external contacts [13]–[16]. Tactile sensing can be useful for such manipulations, especially if it can distinguish among types of events.

In this paper, we present a new tactile sensor aimed at meeting the needs of home robots. It provides a multimodal tactile signal for detecting dynamic contact events as well as monitoring the grasp and load forces. It can also distinguish between linear and rotational sliding. Drawing some inspiration from the way in which multiple mechanoreceptors may be connected to a single neuron, the sensor clusters electrodes to achieve different goals. In the following sections, we describe the design and fabrication of our sensor and explain the method of dynamic reconfiguration. The sensing elements measure localized normal and shear forces and vibratory signatures for slip detection. Using the proposed slip detection methods, a robot was able to estimate minimum required grasping forces of different surface objects within a 1.5 N error. By using rotational slips controlled only by tactile sensing features, the proposed algorithm could reorient and release objects of various mass and surface properties with 78% success rates (Fig. 1).

Manuscript received: Sep, 10, 2019; Revised Dec, 15, 2019; Accepted Jan, 21, 2020.

This paper was recommended for publication by Editor Dan Popa upon evaluation of the Associate Editor and Reviewers' comments.

This paper has supplementary downloadable material available at http://ieeexplore.ieee.org, provided by the authors. This includes movie clips of nib slip behavior, slip detection, and object reorientation.

All authors are with the Center for Design Research, Stanford University, Stanford, CA 94305, USA

Digital Object Identifier (DOI): see top of this page.

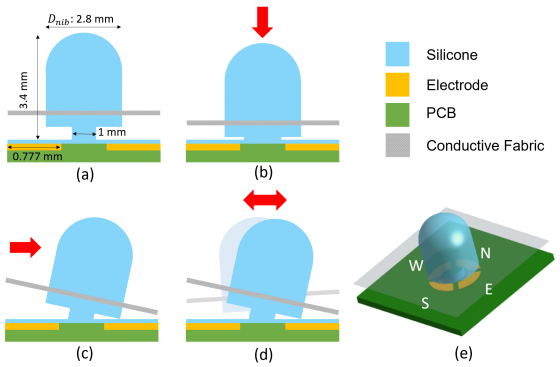

Fig. 2: Cross sectional and isometric view of the proposed design. (a) Idle state. (b) Under normal compression. (c) Under shear force. (d) Vibration under slippage. (e) Overall design

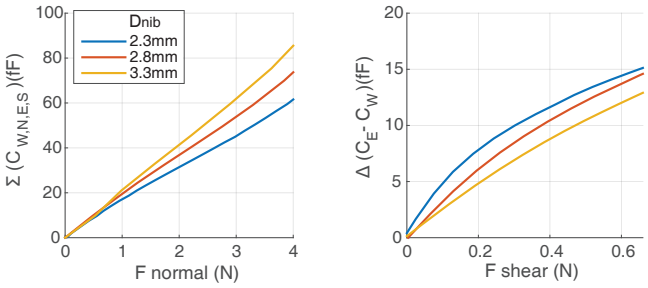

Fig. 3: FEA simulation results for normal and shear loads. Shear load cases are simulated with an initial 4N normal force.

II. Design and Fabrication

A. Working Principle and Design

The proposed sensor has silicone nibs on the skin (Fig. 1), which can displace in compression and bending for a combination of normal and shear sensing. Previous work on multiaxial tactile sensing has adopted a similar approach (e.g. [17]–[19]). The nibs also vibrate when they slip, as do other textures in [12], [20]–[22]. Similar skin patterns have been shown to be good for grasping wet objects [23].

As shown in Fig. 2, a grounded conductive fabric is embedded throughout the nibs. Deflections of the nibs are measured by changes in capacitance in the electrodes beneath. Each nib houses four electrodes, labeled W,N,E,S. The sum of four capacitance values measures normal force (b) and pairs of differentials measure directional shear forces and vibrations (c,d).

We explored how the geometry of nibs affects the sensitivity using a 3D finite element model in COMSOL. We focused especially on nib diameter, D_{nib}, because it represents the unique geometry of our sensor. We fixed the lower body diameter to 1 mm for robust bonding strength and nib center distance to 3.8 mm for reasonable density while maintaining adequate capacitance at each electrode. We fixed nib heights to 3.4 mm for sufficient shear load sensitivity; taller nibs increase the sensitivity while decrease the linearity. We assumed uniform loading from a flat surface contact with friction. As a typical result, Fig. 3 shows that a larger D_{nib} produces greater normal sensitivity but lower shear sensitivity. As a compromise, we chose 2.8 mm for D_{nib}.

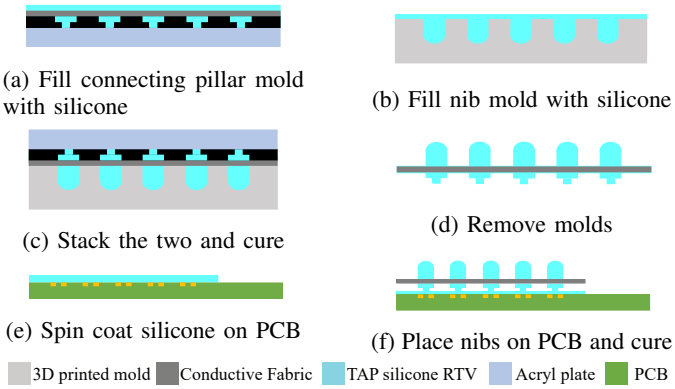

Fig. 4: Sensor fabrication process

Our initial prototype consists of a 6x6 array. The nibs are molded from silicone rubber (TAP, Silicone RTV). To reduce the number of wires yet maintain adequate spatial resolution, electrodes on the same sides of 2x2 clusters of nibs are connected together; in total there are 9 taxels of 2x2 nibs and 4 electrode connections per taxel. On a 4-layer PCB, we wire all connections to each channel input of a capacitance-to-digital converter (CDC) (Cypress, PSoc4200L). In Section III, we discuss how the internal rerouting of electrodes in the CDC enables multimodal sensing from a single device. The overall PCB dimension is 27x41 mm.

B. Fabrication

As shown in Fig. 4, molds for the connecting pillars and nibs are prepared separately. The mold for the pillars is a sheet of acrylic and a polyimide mask (0.254 mm thick) etched and cut with a UV laser (DPSS, Series 3500 UV). A sheet of conductive fabric is primed (Dow, PR-1200 primer red 309G) on both sides and aligned using dowel pins.

The nib mold is 3D printed (Stratasys, Objet30) using VeroWhite resin. Silicone RTV is cast into the mask, through the conductive fabric, and into the nib mold. Next, the silicone is thoroughly degassed to remove microbubbles. Then, the conductive fabric side of the connecting pillar mold is attached on the nib mold and cured to create the nib array. The high viscosity of TAP silicone RTV prevents it from spilling in this process. When the molds are removed after curing, the nib array is ready. To attach the nib array to the sensor, the PCB surface is first primed and spin coated to create a thin layer of silicone. The nib array is aligned with the PCB using dowel pins and placed on the surface. Once the silicone cures, the conductive fabric is connected to the ground electrode of the PCB using silver epoxy and the sensor prototype is ready.

III. Dynamic Reconfiguration of Sensor Clusters

As noted in the Introduction, multiple human mechanoreceptors are often clustered on a single neuron. With this inspiration we implemented dynamic clustering. Our sensor has an embedded microcontroller (PSoc 4200L, Cypress) which connects capacitive sensor electrodes to its CDC module via internal analog switches [24]. By controlling these switches, we customize the electrically connected clusters of

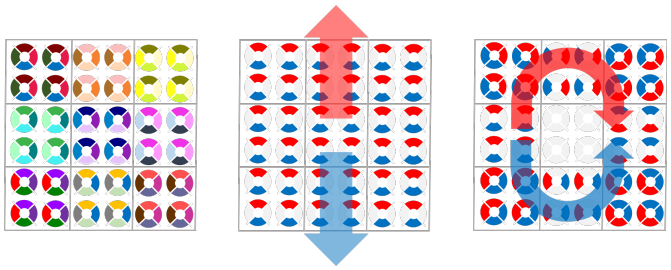

(a) Individual (SI) (b) Linear (FL) (c) Rotational (FR)

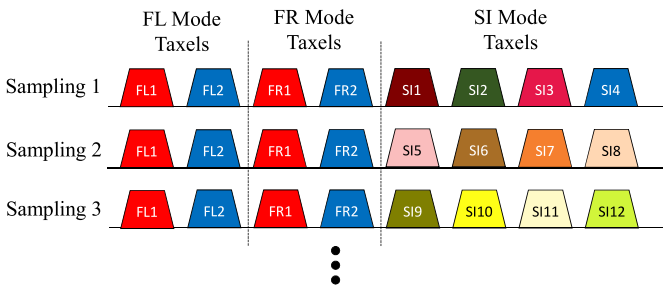

(d) Subsampling sequence

Fig. 5: Reconfigurable sensing modes: (a) Slow Individual sensing (SI), (b) Fast Linear motion sensing (FL), (c) Fast Rotational motion sensing (FR), (d) Sensing modes are dynamically reconfigured within each sample.

the electrodes for each scanning sequence. As an example we demonstrate three different clustering schemes in Fig. 5(a-c) for different modalities: slow individual electrode sensing (SI), fast linear motion (FL), and fast rotational motion (FR). We alternate dynamically among these modes, performing the FL and FR modes more frequently than the SI mode. In SI mode, the sensor scans individual electrodes to monitor local normal and shear stress, which requires a 36 scan sequence. In fast modes (FL, FR) we reduce the number of scans by clustering 9 or 12 electrodes; each mode requires a two scan sequence to produce a differential, as color-coded in Fig. 5. We consider the direction of overall shear stress vectors and cluster electrodes accordingly. The tradeoffs between static and dynamic modes are the sampling bandwidth and spatial resolution. This approach opens a possibility to customize the cluster for different required bandwidths and information.

We present an example of switching three different cluster modes in Fig. 5d. Each sample consists of 8 capacitance scans: 2 of FL, 2 of FR, and a subset of 4 in SI. Because the SI mode has 9 subsets, the effective sampling rate is 1/9 of the others. In this work, the embedded microcontroller is in 13-bit resolution CDC mode, achieving 300 Hz for FL and FR modes and 33.3 Hz for SI; the fast mode sampling rate is chosen at the mechanical bandwidth of the sensor found by an impulse test. The SI mode noise due to the small electrodes is suppressed by a moving average filter with window size 5, still allowing a wider bandwidth than human SA mechanoreceptor [1]. Using this approach, we demonstrate multimodal functionality in the following sections.

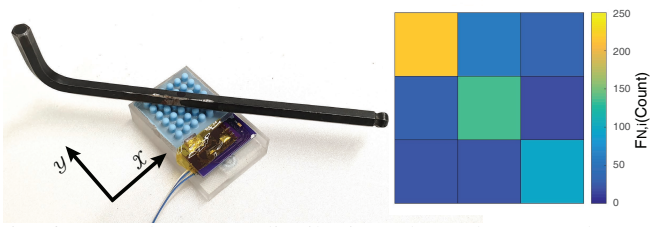

Fig. 6: Normal pressure distribution when a hex wrench (31g) rests on the sensor.

TABLE I: RMS error of sensor calibration (1000 test data). (Input ranges $F_{x,y}$: ±3.5, F_z: 0 ∼ -15 N, $M_{x,y,z}$: ±50 mNm)

Input data set	F_x	F_y	F_z	M_x	M_y	M_z
Uniform	0.12	0.11	0.56	3.0	3.1	1.3
Uniform+Partial	0.15	0.12	1.2	5.1	6.7	1.5

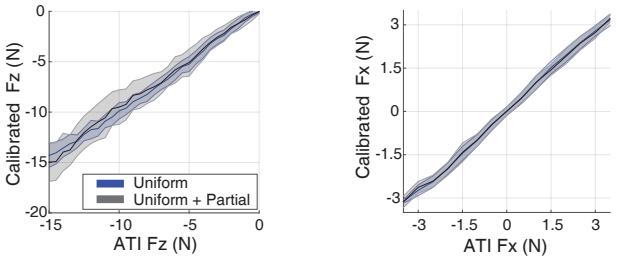

Fig. 7: Distribution of calibrations (4000 train data) in z (left) and x (right). Solid lines are means and shades are error bars.

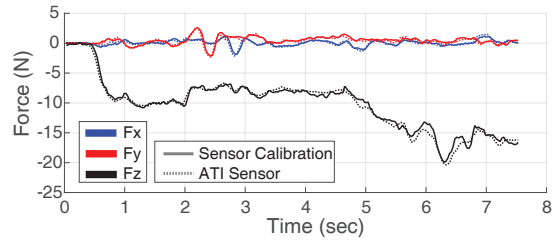

(a) Force Calibration

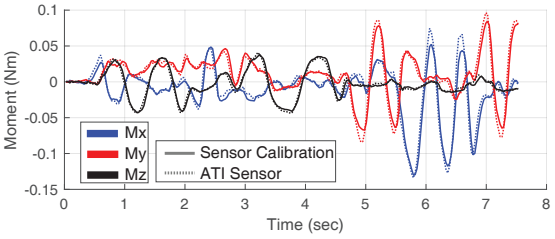

(b) Moment Calibration

Fig. 8: Sensor calibration (uniform loads) compared to ATI.

IV. Sensor Characterization

A. Individual mode, quasi static response

In slow Individual mode, our sensor can measure localized normal and shear stress from compression and bending of nibs on different taxels. From 36 individual capacitance measures, localized normal and shear force are estimated as follows:

$$F_{N,i} \approx C_i(W) + C_i(N) + C_i(E) + C_i(S) \quad (1)$$

$$\vec{F}_{S,i} \approx [C_i(E) - C_i(W)]\hat{x} + [C_i(N) - C_i(S)]\hat{y} \quad (2)$$

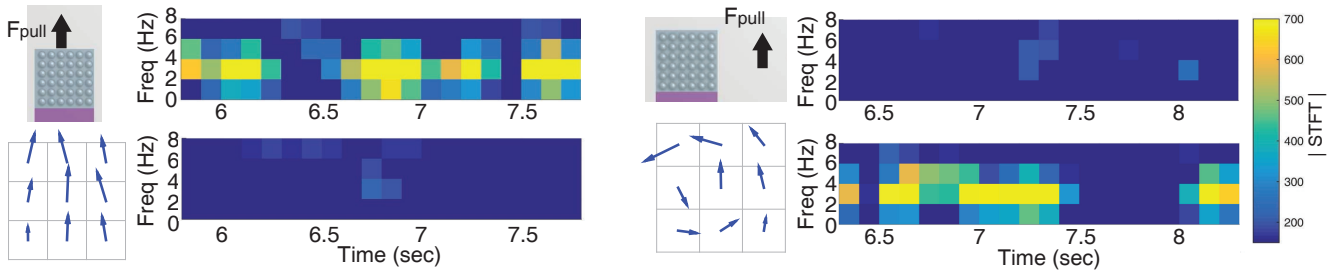

(a) Linear slip, $\nabla \times \vec{F}_S$= 127 (count) (b) Rotational slip, $\nabla \times \vec{F}_S$= 2140 (count)

Fig. 9: Linear (a) and Rotational (b) slip test results on Masonite surface. For each slip, normalized shear force field (left) and STFT of FL(top), FR(bottom) are depicted.

where $F_{N,i}$, $\vec{F}_{S,i}$ are localized normal and shear force estimates, and $C_i(W, N, E, S)$ is a capacitance measure of each electrode at the i^{th} taxel. Fig. 6 shows the measured local normal pressures when the sensor has light normal force (31 g weight). This is useful to locate where contact is made, which may be critical to grasp quality. We demonstrate the use of shear force distributions in the following section.

Because our sensor can measure local stress distributions, it can estimate the overall force and moment from 36 channel readings. To calibrate the sensor, we mounted it on a commercial ATI Gamma F/T load cell and applied randomized forces and moments manually with input ranges as shown in Table I. We applied two load cases: uniform loads with a flat plate and partial loads with a cylinder of 18 mm diameter. A second order polynomial fit results in Table I. Figure 7 shows that calibration without partial loads tracks the resultant F/T input closer than calibration with partial loads. Due to friction and the ability of the nibs to bend in any direction when a surface is pressed against the sensor in the pure normal direction, the repeatibility of the estimated normal force is poorer under large compression, especially with the partial contact and a cylindrical object. However, Fig. 8 shows calibration without partial loads tracks the force/torque load cell readings closely.

Our sensor can distinguish linear and rotational slip in two ways: using the individual mode for estimating load cases and fast sampling modes for vibratory signals. In the individual mode sensing, the shear force vector distribution ($\vec{F}_{S,i}$) produces parallel vector fields in a linear loading cases (Fig. 9a). However, we see vortex-like vector fields in rotational loading cases (Fig. 9b). The vector field can be quantified by the curl ($\nabla \times \vec{F}_S$) about the center taxel. For a dimensionless quantity we take the x, y distance between taxels as a unit length. We use the curl as an initial indicator to distinguish load cases.

B. Linear and Rotational Slip

Using all three modes in Fig. 5, we test differentiating linear and rotational slip. To apply different slip modes, we built a testing apparatus using a muscle lever (Aurora Scientific, 309C), 3 axis linear stage (Zaber, T-LSM50A, T-LSM100A) and a reference F/T sensor (ATI, Gamma SI-32) (Fig. 10). We applied an initial normal grasping force with a linear stage, ranging from 2 to 8N for linear slip and from 5 to 12N for rotational slip. A ramped pull force was applied with the muscle lever; four end loads (1, 2, 5, 8 N) and two ramping

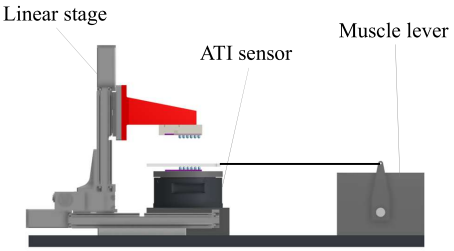

Fig. 10: Test setup for various slip tests

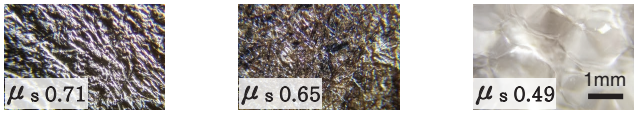

(a) Paper (b) Masonite (c) Wavy Acrylic

Fig. 11: Microscopic view of test surfaces.

periods (2, 5 sec) were used. For the object, we used three flat plates with different friction coefficients and textures as in Fig. 11. For the linear slip test, we aligned our sensor to the muscle lever axis, while for the rotational slip test, we placed the sensor with a 31.75 mm offset; we did not control the moment arm carefully because the ATI F/T sensor measures the applied moments. Slip distance and velocity were measured by the muscle lever.

Another approach to distinguish among slip types is to measure the vibrations of nibs using FL and FR modes. When an object is slipping, we expect a stick/slip motion, resulting in vibrations, as shown in Fig. 2. To monitor the vibration, we implemented a customized short time Fourier Transform (STFT) analysis on the differential signals using a fast Fourier Transform (FFT):

$$\begin{aligned} D_m &= C_{m,1} - C_{m,2} \\ \text{STFT}[t_1, t_2] &= \text{FFT}\{(D_m[t_1, t_2] - fit(D_m[t_1, t_2])) \\ &\quad \times Hamming([t_1, t_2])\} \end{aligned} \tag{3}$$

where D_m is the difference of the capacitance measures of two clusters ($C_{m,1}, C_{m,2}$) in mode m (FL or FR), t_1 and t_2 are the time interval of STFT, and $Hamming$ is a Hamming window with a size of the same interval. fit is a first order polynomial fit; we suppressed the effect of ramping pull forces by subtracting a line that is linearly fitted to the signals in the current time window. From experiments, we found that the effective frequency responses of the nib vibrations reside in the range from 0-8 Hz; thus we chose the time interval of STFT

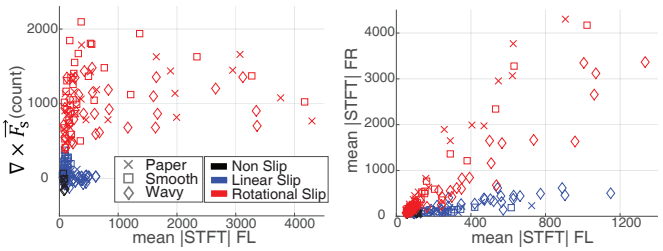

Fig. 12: Slip type distributions with sensor features.

to be 500 ms (a period of 2 Hz sinusoid) and the overlap in the STFT series to be 400 ms, making the STFT output rate close to 8Hz.

From the STFT of the FL and FR modes, our sensor can measure directional vibrations when linear or rotational slip occurs. Fig. 9 shows spectrograms of the STFT from the FL and FR modes while slipping. Because the linear and rotational slips are not completely isolated, there are some frequency responses in both FL and FR caused by both slips. However, the STFT magnitude of FL is significantly greater than FR in linear slip, while FR mode shows a noticeably greater frequency response in rotational slip.

Using the three features, the curl from SI mode and STFT of FL, FR mode, we demonstrate that it is feasible to distinguish among linear slip, rotational slip and no slip. Fig. 12 shows the average magnitude of STFT in the 0-6 Hz for slip and non-slip cases; the slipping pull displacements (∼2mm) for given normal forces were recorded and used as slip criteria. Regardless of the surface type, rotational slips show greater $\nabla \times \vec{F}_S$ and STFT magnitude of FR mode, while linear slip shows less $\nabla \times \vec{F}_S$ and greater STFT magnitude in FL mode. Non-slip cases show lower STFT magnitude in both FL and FR modes. Machine learning is beyond the scope of this paper but it is visually clear that the data are highly distinguishable.

When differentiating slip from non-slip, unlike the average magnitude of STFT, the temporal STFT magnitudes may not be as useful because the vibration is on and off from the stick/slip behavior, which is seen in Fig. 9. We address this issue in the following section.

V. Slip Detection for Regrasp

Applying appropriate grasping force is important for many tasks, for example, handling delicate objects. Humans control and adjust grasping loads using cutaneous tactile sensations, especially for estimating the surface friction coefficient and detecting small slips [2]. For robotic manipulation, studies have included detecting incipient or gross slips to estimate surface properties [22], [25] and readjust grasping loads [5], [9], [25], [26]. When tactile sensors have nibs, detecting and responding to incipient slip is sometimes challenging as the rearrangement of a few nibs could be considered as an incipient slip (requiring more grasp force) when it actually results in an improved grasp force distribution with better contact.

Here, we propose a control algorithm to detect incipient or early stage gross slip using the vibratory signal and stationary normal and shear force measures. We surmise that if F_S/F_N is high, the grasp is more susceptible to gross slips; therefore, even short vibratory signals appeared in STFT should correspond to slip. Conversely, if F_S/F_N is small, Coulomb friction may be sufficient to hold the object, in which case momentary vibratory signals may correspond to a local rearrangement of nibs.

Algorithm 1: Linear slip detection

```
flagCounter = 0;
CounterMax = f(F_S/F_N);
while flagCounter < CounterMax do
    Update CounterMax;
    if Mag(STFT) > SLIP_THRES then
        flagCounter++;
    end
    if Time after last flag > TIME_THRES then
        flagCounter−−;
    end
end
Slip Detected;
```

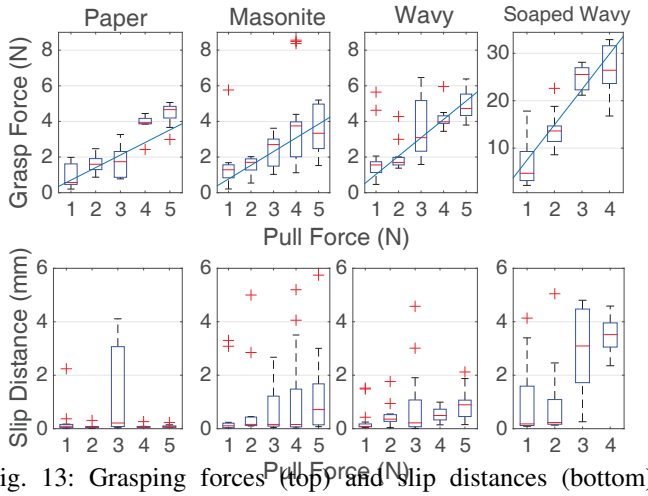

Fig. 13: Grasping forces (top) and slip distances (bottom) when slip is detected from Algorithm 1. Solid lines in the top graphs are the minimum required grasping forces ($F_{G,req}$).

TABLE II: Slip Detection results

	Paper	Smooth Masonite	Wavy Acrylic	Soaped Wavy
	Mean ($(\lvert F_{G,slip} - F_{G,req} \rvert)$ (N)			
All Detection	0.77	1.06	0.84	3.44
Gross Slip	0.55	1.05	0.51	3.22
Detection Success (<6mm)	$\frac{57}{58}$	$\frac{67}{74}$	$\frac{61}{61}$	$\frac{62}{68}$

To test this approach, we used the setup of Fig. 10 to apply a decreasing normal force while keeping the pull force constant, finding the normal force level when the plate is about to slip. We used a set of plates as in Table II adding one very slippery surface of a soaped wavy acrylic sheet (μ_s: 0.07). The initial normal load was set to hold the test plate tightly and release the compression by 0.03 mm/s which decreases the normal force by approximately 0.3 N/s. While reducing the normal force,

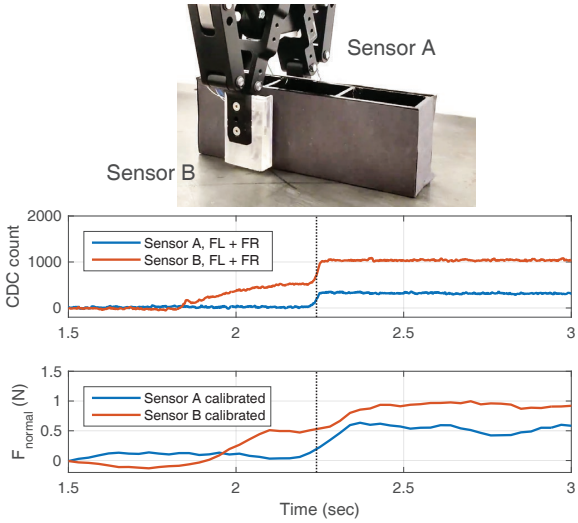

Fig. 14: Detecting an initial contact on both sensors using the sum of FL and FR (top) compared to the calibrated force from SI mode(bottom). Dotted line is when stop closing command sent.

we ran a slip detection algorithm as shown in Algorithm 1. For proof of concept, we only applied the algorithm to the linear slip mode, which can be extended in similar manner to rotational slip. In Algorithm 1, the STFT threshold flag is accumulated up to a positive integer $CounterMax$ where it claims detection of slip; $CounterMax$ is negatively proportional to the ratio between shear and normal force sensing as follows:

$$CounterMax = f(\frac{F_S}{F_N}) = M - \alpha \frac{F_{S,y}}{\sum F_{N,i}} \quad (4)$$

where M is maximum of $CounterMax$ and α is a weight of the shear-normal force ratio. Pull force is assumed to be aligned to the y axis. We tuned M and α as 9 and 10 from experiments. The pull force range was 1-5 N and the grasping force was measured using the ATI F/T sensor.

Fig. 13 shows the measured grasp force and slip distance when slip distance is less than 6 mm, which is assumed a safe detection. The safe detection success rate is 94.6% as shown in Table II. The grasping forces at slip detection ($F_{G,slip}$) are close to the minimum required grasping force($F_{G,req}$) estimated from the static friction coefficients (μ_s, measured), resulting in overall 1.5 N of difference between them (Table II). For readjustment of grasping force, we considered gross slip detection cases, where $F_{G,slip}$ is less than $F_{G,req}$; their average difference is 1.3 N. This result suggests that a controller could increment grasping force of minimum 1.3 N to stop slips if it detects slip using Algorithm 1. We showed an example of recovery control using the current setup in the supplementary video; however, the response time of our gripper is not sufficient to demonstrate a complete solution, which we leave as future work.

The variance of slip distance and force on smooth masonite fiberboard and wavy acrylic are somewhat larger due to the lack of a smooth microtexture. We believe that with a more conservative parameter tuning, Algorithm 1 should perform better when dealing with smooth objects. The algorithm performs acceptably on the soaped wavy surface with higher slip distances, which should be attributed to the macroscopic texture. In the case of paper surfaces, a pull force of 3 N shows much higher variance in slip distance; we think the current parameter for Algorithm. 1 is too forgiving for this load case. A more sophisticated method for tuning the parameters, such as machine learning, should find more appropriate parameters.

Algorithm 2: Reorientation - Adjust Grasping Force

```
Start closing Gripper;
if both Sensor A,B ∑_{i=1}^{2} C_{FL,i} + C_{FR,i} >
 CONTACT_THRES then
    Stop closing Gripper;
end
Start lifting robot arm;
while Lifting to MidPoint do
    if Mag(STFT_FL 0-6Hz) > FL_SLIP_THRES then
        Increment Grasping force;
        Wait for TIME_SETTLE
    end
end
Grasping Force Adjusted;
```

Algorithm 3: Reorientation - Lift-Rotate Object

```
Start lifting robot arm;
while Lifting to TargetPoint do
    if Mag(STFT_FR 0-6Hz) < FR_SLIP_THRES then
        Decrement Grasping force;
    end
    if Mag(STFT_FR 6-8Hz) > FR_UPRIGHT_THRES
     then
        Stop Lifting Robot Arm;
    end
end
Upright Orientation Detected;
```

VI. Object Reorientation using Rotational Slip

The ability for a robot to reorient grasped objects can significantly expand its dexterity in confined spaces. For humans, a common strategy is to use rotational slip while keeping the grasping force sufficient to prevent or minimize linear slip. Grasp control for rotational slip and reorientation has been studied (e.g. [13], [15], [16]) and a specified gripper design for such tasks has been demonstrated [27]. We propose control algorithms for reorienting an object as shown in Fig. 1, using the fast linear and rotational (FL and FR) signals. Because it relies on directional slip sensing, the algorithm is relatively insensitive to the inertia of the object. For the following experiment descriptions, we used an industrial 2 finger gripper (Robotiq, 2F-85) and a 6 DOF robot (Universal UR5-CB2). Our sensors were attached to the finger pads. For the object, we made an acrylic box (155x33x54 mm, 118 g) with 3 bins in which to place weights for different inertias and centers of mass. The surface was covered with paper as in Table II for increased friction.

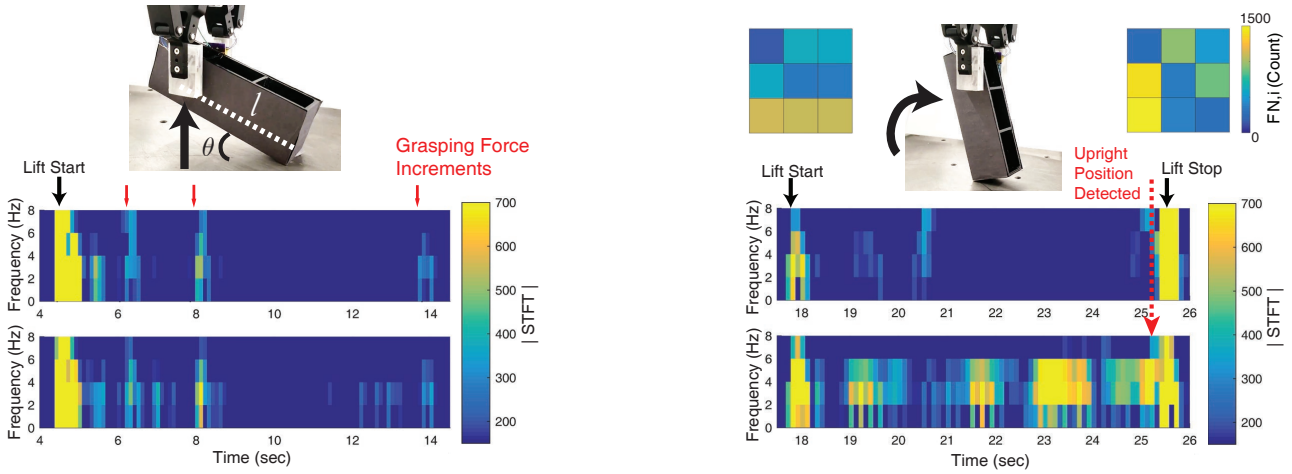

(a) Adjust Grasping Forces (Algorithm.2)

(b) Lift-Rotate Object (Algorithm.3)

Fig. 15: STFT analysis of FL mode (Top) and FR mode (Bottom) for adjusting grasping force (a), and reorienting using rotational slips (b). Inset pressure map in (b) shows changes of local contacts during manipulation.

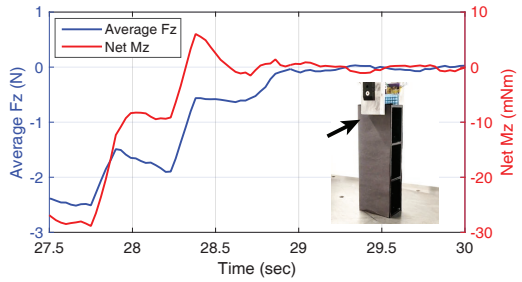

Fig. 16: Calibrated normal force and torsional moment while gently releasing the object.

The algorithm consists of three parts: applying an appropriate grasping force, maintaining rotational slip and detecting an upright position, and releasing the object gently. When applying the grasping force, we assumed that a force that just prevents linear slip will allow rotational slips. We use (Algorithm 2) to induce linear slips from a gentle initial touch, gradually increasing the grasping force until no linear slip is detected. For gentle initial contact, we relied on the capacitance sum of FL and FR clusters rather than the calibrated SI mode because of its faster response and sharper change (Fig. 14). While lifting the gripper slowly (2 to 5 mm/s) after initial touch, the STFT of the FL mode produces a signal to increment the grasping force if its magnitude exceeds a threshold (Fig. 15a). For simplicity we used slip detection of Algorithm 2 rather than using the algorithm introduced in Section V.

After the gripper reaches the midpoint, the robot arm lifts the gripper faster (10 mm/s) until the object reaches the upright position (Algorithm 3). While lifting, the controller checks the STFT of FR mode to maintain rotational slip; if it does not rotate, the controller decrements the grasping force. An upright position can be detected from simple kinematics of the supported object. When the contact point lifts at constant speed, v, the angular speed of the object, $\dot{\theta}$, is

$$\dot{\theta} = \frac{v}{l \cos\theta} \tag{5}$$

where θ is the angle between the object and the support surface and l is the distance between the gripper and the object-surface contact point, as shown in Fig. 15a. As θ approaches to 90 deg, the angular speed becomes higher, which appears in strong magnitude of STFT in a higher frequency band (6-8 Hz).

TABLE III: Reorientation-Release Success Rate

Different Weights with COM at $\frac{1}{2}$L (Paper)	100g	200g	300g
	9 / 11	10 / 11	7 / 11
Different COM with 200g with the Paper surface	$\frac{1}{3}$L	$\frac{1}{2}$L	$\frac{2}{3}$L
	11 / 11	10 / 11	3 / 11
Different surfaces with 200g at $\frac{1}{2}$L	Paper	Masonite	Wavy
	10 / 11	10 / 11	10 / 11

After the object reaches an upright position, we show that the controller can gently release the object by moving the gripper forward while decrementing grasping forces until the calibrated normal force and torsional moment diminish as shown in Fig. 16. It is also possible to regrasp the object firmly after reaching the upright position for a subsequent manipulation task.

Table III shows that the proposed algorithm can reorient the object decently without knowing its weight, center of mass (COM), and surface; overall success rate is 78%. The poorest success rate occurs when COM is above the geometric center; the reorientation mostly succeeded but the object tips over when the gripper releases it. The success rate will increase if more sophisticated release control is used, for example a vision-tactile control [28].

VII. Conclusion

We present a dynamically reconfigurable tactile sensor that enables directional multimodal sensing. For sensing multiaxis forces and vibratory signals, and potentially for better grip on wet or slippery objects, our sensor is covered with rounded silicone nibs. Deflections of each nib change capacitance between the embedded conductive fabric and four electrodes underneath; sums and differences of capacitance measure local normal and shear pressures, and directional nib vibrations. The

electrode connections are rerouted inside the CDC chip, which allows clustering multiple electrodes for fast compressed sampling and selectivity of directional signals. We propose three modes, corresponding to electrode clusters (SI, FL, FR), for sensing static local pressures and fast linear/rotational motion; our subsampling method switches modes dynamically. Although this sensor is not intended to replace a force/torque load cell, it is convenient to compare its resultant force and moment to those from a commercial 6-axis sensor. The results match relatively well (Fig. 8), but variability in how the nibs bend in response to a normal load affects the repeatability, especially in contact with curved objects.

We demonstrate that features of the modes can be used to distinguish among nonslip, linear slip, and rotational slip. Using linear slip signals and static force measures, we present a controller to detect onset of slip for readjusting grip forces; the controller detects slips on different surface types with 1.5 N of grasping force margin from the minimum required amount. We also demonstrate a controller to reorient an object using rotational slips controlled only by the tactile sensor features; the success rate of reorient-release is 78% for different inertia and surface types.

As future work, larger arrays of sensing elements can be implemented on flexible multilayer circuits to cover curved robotic surfaces. The dynamic reconfiguration can also create a customized first-order neural network for effective event detection [3] and object recognition [29]. The proposed tactile sensing method also can be integrated with other type of sensors, such as inertial measurement units (IMU) or vision [28], to provide data sets for machine learning, which may allow grasp force control on various objects without hand tuning.

VIII. Acknowledgement

Toyota Research Institute provided funds to assist the authors with their research; this article solely reflects the opinions and conclusions of its authors and not TRI or any other Toyota entity. T. M. Huh is additionally supported by a Samsung Scholarship and H. Choi is supported by the Kwanjeong Fellowship. This work is also supported in part by the Beijing Institute of Collaborative Innovation (BICI).

References

[1] R. S. Johansson and J. R. Flanagan, "Coding and use of tactile signals from the fingertips in object manipulation tasks," *Nature Reviews Neuroscience*, vol. 10, no. 5, p. 345, 2009.

[2] R. S. Johansson and G. Westling, "Roles of glabrous skin receptors and sensorimotor memory in automatic control of precision grip when lifting rougher or more slippery objects," *Experimental brain research*, vol. 56, no. 3, pp. 550–564, 1984.

[3] J. A. Pruszynski, J. R. Flanagan, and R. S. Johansson, "Fast and accurate edge orientation processing during object manipulation," *Elife*, vol. 7, p. e31200, 2018.

[4] P. Dario and D. E. De Rossi, "Composite, multifunctional tactile sensor," Dec. 3 1985, uS Patent 4,555,953.

[5] J. M. Romano, K. Hsiao, G. Niemeyer, S. Chitta, and K. J. Kuchenbecker, "Human-inspired robotic grasp control with tactile sensing," *IEEE Transactions on Robotics*, vol. 27, no. 6, pp. 1067–1079, 2011.

[6] P. Mittendorfer and G. Cheng, "Humanoid multimodal tactile-sensing modules," *IEEE T-RO*, vol. 27, no. 3, pp. 401–410, 2011.

[7] N. Salowitz, Z. Guo, Y.-H. Li, K. Kim, G. Lanzara, and F.-K. Chang, "Bio-inspired stretchable network-based intelligent composites," *Journal of Composite Materials*, vol. 47, no. 1, pp. 97–105, 2013.

[8] S. Harada, K. Kanao, Y. Yamamoto, T. Arie, S. Akita, and K. Takei, "Fully printed flexible fingerprint-like three-axis tactile and slip force and temperature sensors for artificial skin," *ACS nano*, vol. 8, no. 12, pp. 12 851–12 857, 2014.

[9] Z. Su, K. Hausman, Y. Chebotar, A. Molchanov, G. E. Loeb, G. S. Sukhatme, and S. Schaal, "Force estimation and slip detection/classification for grip control using a biomimetic tactile sensor," in *Humanoids*. IEEE, 2015, pp. 297–303.

[10] A. Maslyczyk, J.-P. Roberge, V. Duchaine *et al.*, "A highly sensitive multimodal capacitive tactile sensor," in *ICRA*, 2017, pp. 407–412.

[11] Q. Hua, J. Sun, H. Liu, R. Bao, R. Yu, J. Zhai, C. Pan, and Z. L. Wang, "Skin-inspired highly stretchable and conformable matrix networks for multifunctional sensing," *Nature comm.*, vol. 9, no. 1, p. 244, 2018.

[12] B. Heyneman and M. R. Cutkosky, "Slip classification for dynamic tactile array sensors," *IJRR*, vol. 35, no. 4, pp. 404–421, 2016.

[13] D. L. Brock, "Enhancing the dexterity of a robot hand using controlled slip," in *ICRA*. IEEE, 1988, pp. 249–251.

[14] R. R. Ma and A. M. Dollar, "On dexterity and dexterous manipulation," in *ICAR*. IEEE, 2011, pp. 1–7.

[15] R. H. N. Chavan-Dafle and A. Rodriguez, "In-hand manipulation via motion cones," in *RSS*, 2018.

[16] Y. Hou, Z. Jia, and M. T. Mason, "Fast planning for 3d any-pose-reorienting using pivoting," in *ICRA*. IEEE, 2018, pp. 1631–1638.

[17] H.-K. Lee, J. Chung, S.-I. Chang, and E. Yoon, "Normal and shear force measurement using a flexible polymer tactile sensor with embedded multiple capacitors," *Journal of Microelectromechanical Systems*, vol. 17, no. 4, pp. 934–942, 2008.

[18] E. Choi, S. Hwang, Y. Yoon, H. Seo, J. Lee, S. Yeom, G. Ryu, H. Yang, S. Kim, O. Sul *et al.*, "Highly sensitive tactile shear sensor using spatially digitized contact electrodes," *Sensors*, vol. 19, no. 6, p. 1300, 2019.

[19] P. Yu, W. Liu, C. Gu, X. Cheng, and X. Fu, "Flexible piezoelectric tactile sensor array for dynamic three-axis force measurement," *Sensors*, vol. 16, no. 6, p. 819, 2016.

[20] Y. Jiang, Z. Ma, B. Cao, L. Gong, L. Feng, and D. Zhang, "Development of a tactile and slip sensor with a biomimetic structure-enhanced sensing mechanism," *J. Bionic Engineering*, vol. 16, no. 1, pp. 47–55, 2019.

[21] H. Khamis, R. I. Albero, M. Salerno, A. S. Idil, A. Loizou, and S. J. Redmond, "Papillarray: An incipient slip sensor for dexterous robotic or prosthetic manipulation–design and prototype validation," *Sensors and Actuators A: Physical*, vol. 270, pp. 195–204, 2018.

[22] M. R. Tremblay and M. R. Cutkosky, "Estimating friction using incipient slip sensing during a manipulation task," in *ICRA*. IEEE, 1993, pp. 429–434.

[23] K. Mizushima, T. Nishimura, Y. Suzuki, T. Tsuji, and T. Watanabe, "Surface texture of deformable robotic fingertips for a stable grasp under both dry and wet conditions," *IEEE Robotics and Automation Letters*, vol. 2, no. 4, pp. 2048–2055, 2017.

[24] V. Kremin, "Capacitance to code converter with sigma-delta modulator," Oct. 6 2015, uS Patent 9,154,160.

[25] C. Melchiorri, "Slip detection and control using tactile and force sensors," *IEEE/ASME TMECH*, vol. 5, no. 3, pp. 235–243, 2000.

[26] M. Stachowsky, T. Hummel, M. Moussa, and H. A. Abdullah, "A slip detection and correction strategy for precision robot grasping," *IEEE/ASME TMECH*, vol. 21, no. 5, pp. 2214–2226, 2016.

[27] N. Chavan-Dafle, M. T. Mason, H. Staab, G. Rossano, and A. Rodriguez, "A two-phase gripper to reorient and grasp," in *CASE*. IEEE, 2015, pp. 1249–1255.

[28] M. A. Lee, Y. Zhu, K. Srinivasan, P. Shah, S. Savarese, L. Fei-Fei, A. Garg, and J. Bohg, "Making sense of vision and touch: Self-supervised learning of multimodal representations for contact-rich tasks," in *ICRA*. IEEE, 2019, pp. 8943–8950.

[29] C. W. Zhao, M. J. Daley, and J. A. Pruszynski, "Neural network models of the tactile system develop first-order units with spatially complex receptive fields," *PloS one*, vol. 13, no. 6, p. e0199196, 2018.